

See discussions, stats, and author profiles for this publication at: <https://www.researchgate.net/publication/391954100>

Direct Estimation of Earthquake Source Properties from a Single CCTV Camera

Preprint · May 2025

DOI: 10.48550/arXiv.2505.15461

CITATIONS

0

READS

16

7 authors, including:



Mathias Lebihain

École nationale des ponts et chaussées

25 PUBLICATIONS 263 CITATIONS

[SEE PROFILE](#)



François X. Passelègue

French National Centre for Scientific Research

59 PUBLICATIONS 1,426 CITATIONS

[SEE PROFILE](#)

Direct Estimation of Earthquake Source Properties from a Single CCTV Camera

Soumaya Latour^{1†}, Mathias Lebihain², Harsha S. Bhat³,
Cédric Twardzik⁴, Quentin Bletery⁴, Kenneth W. Hudnut⁵, François Passelègue^{*4†},

¹Université de Toulouse, CNRS, Observatoire Midi-Pyrénées, IRAP, Toulouse, France.

²Navier, ENPC, Institut Polytechnique de Paris, Univ Gustave Eiffel, CNRS, Marne-la-Vallée, France.

³Laboratoire de Géologie, École Normale Supérieure, CNRS, UMR 8538, PSL Université, Paris, France

⁴Université Côte d'Azur, CNRS, Observatoire de la Côte d'Azur, IRD, Géoazur, Sophia Antipolis, France.

⁵Southern California Edison, Rosemead, 91770, CA, United States.

*Corresponding author. Email: francois.passelegue@cnrs.fr

†These authors contributed equally to this work.

We present the first direct measurement of the slip-rate function during a natural coseismic rupture, recorded during the 28 March 2025, M_w 7.7 Mandalay earthquake (Myanmar). This measurement was made on a video footage of the surface rupture captured by a security camera located only meters away from the fault trace. Using direct image analysis, we measured the relative slip at each time step and deduced the slip rate. Our results show a local slip duration of 1.3 s, and that the surface slip velocity peaked at nearly ≈ 3 m/s during the passage of the slip front, with a cumulative slip of approximately ≈ 3 m. These findings demonstrate the pulse-like nature of the seismic rupture, at least at the location of the recording. Using analytical rupture models, we obtain the complete mechanical properties of this pulse including the energy release rate.

Abstract

Introduction

Estimating the spatial and temporal evolution of slip along fault interfaces is critical for understanding the physics of deformation processes in the Earth's crust throughout the seismic cycle (1). Because slip typically occurs at depth under extreme conditions, direct in-situ observations are in most cases impossible. Therefore, reconstructions of slip history rely on inverse modeling (2). Consequently, our understanding of earthquake physics is fundamentally limited by the resolution and coverage of the data used in these inversions, as well as the inherent complexity of the forward problem (3, 4, 5, 6).

On March 28, 2025, a devastating M_w 7.7 earthquake struck Myanmar along the Sagaing Fault (10) near Mandalay. The earthquake caused catastrophic damage: more than 5,400 fatalities, over 11,000 injuries, and thousands reported missing. Infrastructure losses included 120,000 homes, 2,500 schools, numerous temples, and key transportation networks such as bridges and airports. Several historic sites, particularly in Inwa, suffered extensive damage. This right-lateral strike-slip event ruptured over 450 km of the fault, with slip reaching the surface on long segments, and horizontal displacements reaching up to 6 meters (Figure 1a (7)). The moment source function derived from USGS indicates that the rupture propagation lasted approximately 120 seconds (Figure 1b), in agreement with the SCARDEC solution (9), and likely included supershear phases (11).

From a scientific standpoint, this earthquake is remarkable for providing the first real-time visual recording of surface rupture. It was captured at a solar power station by a security camera, located only meters away from the surface rupture trace (Figure 1a), 124 km south of the epicenter. Here, we present an analysis of this video recording (see supplementary material), which allows us to directly measure, for the first time, the slip and slip-rate functions on a fault point during a natural earthquake. Then, we use the slip-rate function to discuss the implications for dynamic and kinematic rupture parameters.

Measurement of local slip rate during the earthquake

The camera is positioned on the east side of the fault and is approximately oriented in the southwest direction. To estimate the local slip rate, we tracked distinct visual landmarks located on both sides of the fault (Figure 2a). The primary reference point is a concrete or metallic pillar ($R0$) located on the west side of the fault, while two additional landmarks $R1$ and $R2$ are small poles located adjacent to a road and behind a fence composed of vertical bars. Throughout the video, these features display predominantly horizontal motion relative to the foreground, consistent with right-lateral strike-slip faulting.

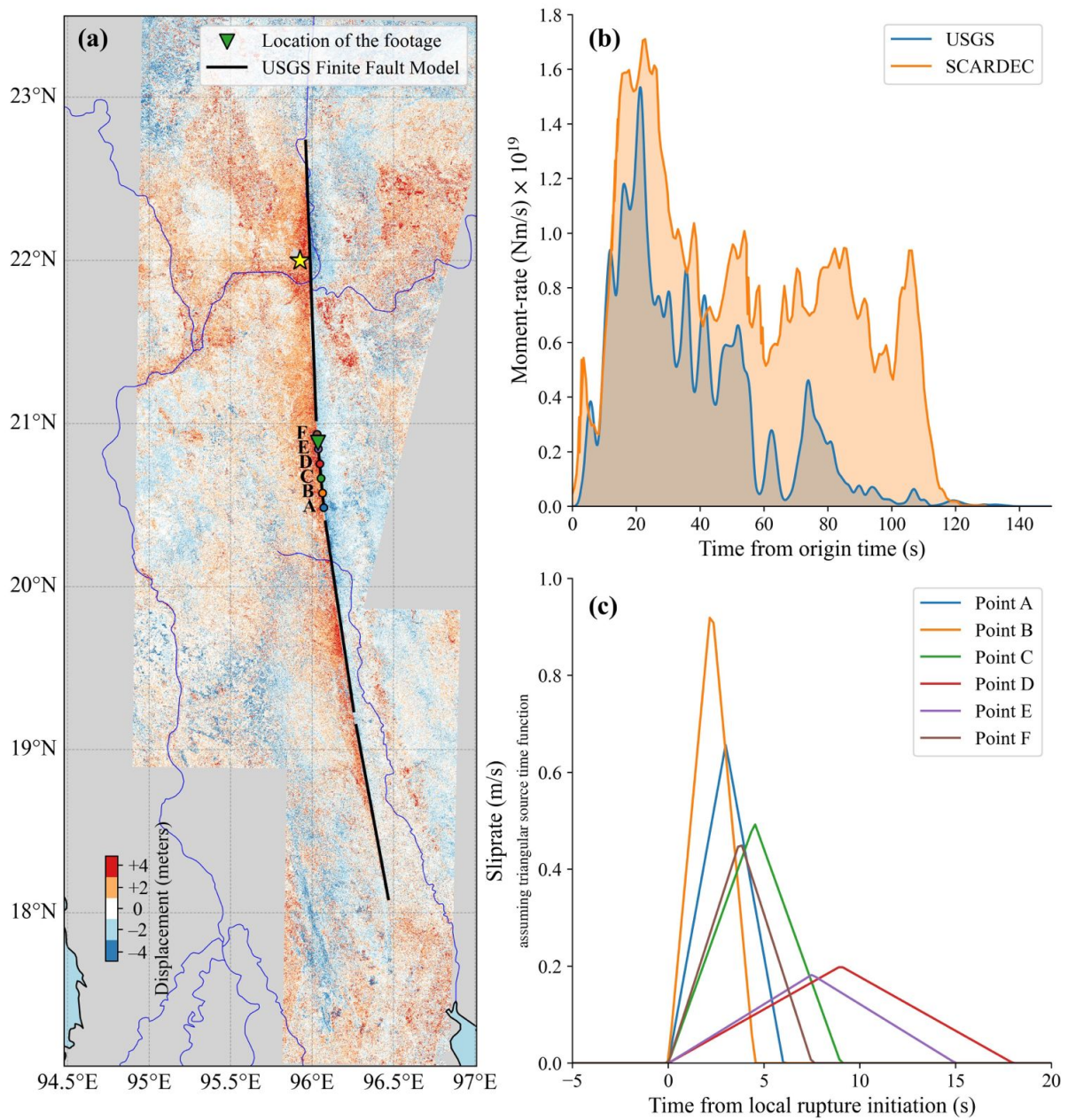


Figure 1: (a) North-south displacement field derived from the sub-pixel correlation of Sentinel-2 optical imagery (7). The yellow star indicates the location of the epicentre, while the green triangle marks the location of the footage, as given in the YouTube video description. The black lines show the surface trace of the finite fault model obtained from the USGS (8). The dots labelled A to F show the locations of the shallowest subfaults of the USGS finite fault model, which were used to extract the local slip-rate functions shown in (c). (b) Moment-rate functions from the USGS (8) and SCARDEC (9). (c) Local slip-rate functions derived from the USGS finite fault model. This was only done for the shallowest subfaults of the segment highlighted in (a). Note that we use a triangular function to display the local slip-rate function instead of the asymmetric cosine function used by the USGS for the kinematic inversion.

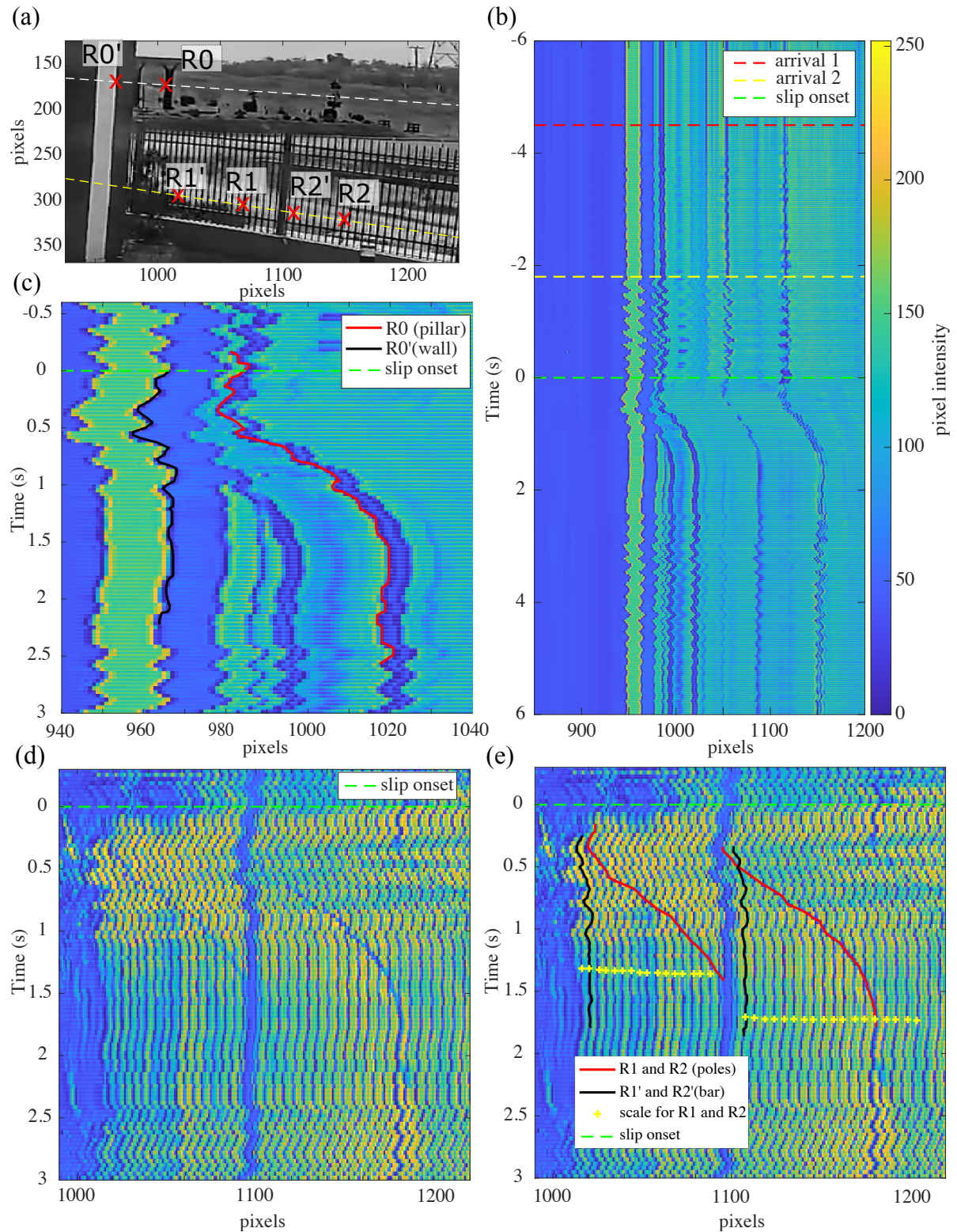


Figure 2: Landmarks tracking method. (a) Zoom on a frame of the video during the slip. The landmarks are indicated (R0: pillar; R1: pole moving behind the fence, R2: other pole behind the fence), and the objects used as reference for each (R0': wall of the arch, R1' and R2': bar of the fence close to the initial position of R1 and R2). White dashed line: Line 1 for projection of figures 2b and 2c. Yellow dashed line: Line 2 for projection of panels (d) and (e). (b) and (c) motion along line 1 and tracking of R0 and R0' (d) and (e) motion along line 2 and tracking of R1, R1', R2, and R2'

To quantify this motion, we defined two fault-parallel lines intersecting the vertical landmarks and tracked the pixel intensity along these lines over the entire duration of observable rupture propagation (Figure 2b,c,d,e). We define $t = 0$ s as the onset of fault slip. Ground shaking begins at $t = -4.5$ s, evident as coherent motion across the frame due to camera shaking. A secondary seismic phase is observed at approximately $t = -1.8$ s. The onset of fault slip is identified as the moment when the tracked landmarks begin to move relative to nearby, foreground features. This relative motion continues until approximately $t = 1.6$ s (Figure 2c).

For each landmark, we selected a nearby visually stable reference point on the east side of the fault, as shown in Figure 2a: $R0'$ (a vertical wall), and $R1'$, $R2'$ (vertical bars of the fence). We tracked the motion of both the landmark and its corresponding reference feature over time (Figure 2c,e). The difference in their pixel positions provides a measure of relative displacement that is corrected for camera motion. This approach yields a temporal resolution of 0.33 s and a spatial resolution with a relative uncertainty of approximately $\pm 20\%$.

The slip history derived from the three measurements is shown in Figure 3a. The curve obtained from $R0$ provides the most reliable estimate, as both the onset and arrest of motion are clearly visible in the video. The timing and slope of the estimates from $R1$ and $R2$ are consistent with that of $R0$. The slip increases smoothly from 0 to 3 m over approximately 1.3 s, after which it ceases. The slip-rate function (Figure 3b) was obtained by numerically differentiating the slip history after resampling it at 90 Hz. A moving average with a 0.33 s time window was then applied, as we interpret the oscillations in the raw curve to result from uncertainties in manual tracking and from imperfect correction of camera motion. The slip-rate function is slightly asymmetric: the slip rate rises rapidly from 0 to 3 m/s within 0.6 s, then decreases more gradually to 0 over approximately 1 s. These values correspond to a slip acceleration of 5 m/s^2 and a deceleration of 3 m/s^2 .

The total slip duration is best estimated using the rise time of the slip function, as the smoothing applied during signal processing tends to artificially broaden the slip-rate pulse. The most robust estimate of slip duration is 1.3 s (Figure 3a), and it is independent of any assumptions related to spatial scaling. In contrast, our estimates of total and intermediate slip are more uncertain, due to a relative uncertainty of approximately 20 % in the spatial scaling factor (Figure S1), which must be considered when interpreting the results. Alternatively, it is possible that the video footage does not capture the entire rupture process; a secondary slip pulse may have occurred after the visible event. Moreover, the duration of the video prevents any assessment of potential post-seismic deformation, such as afterslip, which may have contributed significantly to fault slip in the hours following the mainshock. The uncertainty in total slip also affects the absolute values of the slip rate.

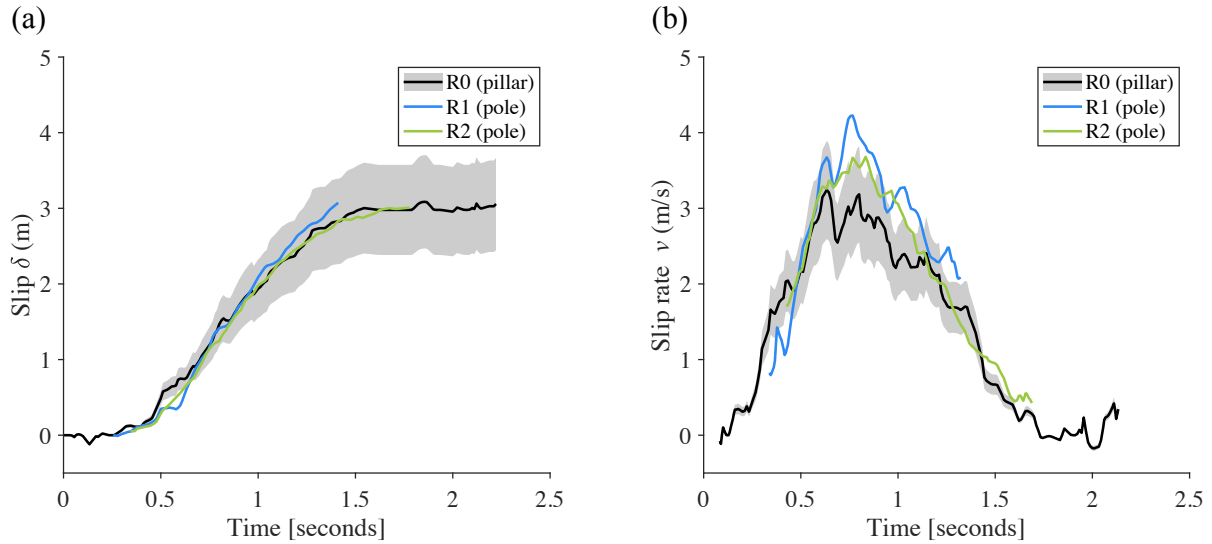


Figure 3: (a) Evolution of the fault slip during the rupture propagation modeled using the three different reference points (Figure 2a). (b) Slip-rate function derived from (a) for the three different references. The gray shaded areas in (a) and (b) represent the effect of the 20% uncertainty in our slip estimate on the measurements derived from R0, which is the reference used in the modeling.

Duration and shape of the slip rate function

While our absolute slip and slip-rate measurements may be influenced by a factor 0.8 to 1.2 by assumptions made to conduct our image analysis, our measurement of the duration and the evolution of the slip are robust. Our results demonstrate that the local slip duration of 1.3 s is much shorter than the total rupture duration of 100 – 120 s (Figure 1b). This clearly shows that this rupture has a pulse-like nature, also called self-healing pulse, at least at the surface in this segment of the fault. Self-healing pulse has long been identified as a possible mode of earthquake rupture (12). In fact, pulse-like behavior appears to be a fairly common feature of rupture models of large earthquakes (13). The origin of this pulse-like behavior can be attributed to the elongated geometry of the rupture. In the case of the Mandalay earthquake, the rupture is expected to have quickly saturated the seismogenic width, resulting in a large length-to-width ratio at the footage location. Under these conditions, it is expected that a pulse-like rupture will emerge naturally (14, 15).

As previously stated, our results demonstrate that fault slip occurred within a narrow time window of approximately 1.3 s, with a peak slip rate of ≈ 3 m/s. These values are consistent with coseismic slip rates expected during large earthquakes. Particle velocity in the vicinity of the fault was predicted to be capable of reaching several meters per second for self-healing pulse ruptures (12). Note that our direct measurements of the fault slip rate are much higher than those inverted from teleseismic data at this site (8), which indicate a peak slip rate on the order of 0.2 m/s at the site location (Figure 1c). In addition, the duration of the slip is much shorter than the inverted one: 1.3 s against ≈ 16 s for the USGS kinematic

model. But, it is well known that modeling the rupture process involves significant uncertainty (16, 6), which could explain this difference. In fact, the inverted slip duration just 10 km north of the site location decreases from ≈ 16 s to ≈ 6 s (Figure 1c). The same applies to the peak slip rate. Nevertheless, this discrepancy underscores the value of this direct observation: our analysis not only provides the first direct measurement of the slip-rate function during a natural earthquake, but also offers an empirical benchmark for validating and refining seismic source models of large earthquakes.

The shape of the slip-rate function is a key parameter in kinematic slip models (17) and plays an important role in ground motion prediction (18). In this study, the smoothed slip-rate function exhibits a simple form that can be described as an asymmetric triangle, with the acceleration phase duration approximately 60% that of the deceleration phase. A similarly smooth, asymmetric triangular slip-rate function has been observed in friction experiments involving self-healing slip pulses propagating at 0.76 times the Rayleigh wave speed (19).

An analytical form of the slip-rate function was proposed for mode III self-healing pulses (20). This form, sometimes referred to as the Yoffe function, is characterized by an infinitely steep onset, a sharply peaked maximum, and a long tail with a variable slope. Although the Yoffe function qualitatively captures the asymmetry observed in our data, its overall shape is too peaked and excessively asymmetric. A regularized version of the Yoffe function, derived from dynamic rupture models (21), more closely resembles the slip-rate function observed in our measurements, though it still exhibits greater asymmetry. This first direct measurement of the slip-rate function thus provides valuable empirical constraints for the development of improved rupture models for large earthquakes.

Implications for local rupture speed

The rupture is propagating southward along this segment of the fault. Although we did not directly observe the rupture front in the video, there appear to be two consecutive frames between which the rupture front advances southward. However, due to the high rupture velocity, the low frame rate, and the limited resolution of the footage, it is not possible to make a definitive observation, particularly given the emergent nature of the slip function. Moreover, the camera's internal clock is not synchronized with official timing: the timestamps embedded in the footage are approximately four minutes earlier than the event origin time reported by the USGS (8). This discrepancy prevents any direct estimation of the local or average rupture velocity from the video recording.

Kinematic models have proposed supershear rupture propagation along this segment of the fault (8, 11). However, the second observed arrival, occurring approximately 1.8 s before the onset of slip, clearly

induces horizontal ground shaking in the fault-normal direction. This motion is indicative of S-wave arrivals and suggests that, at this location, the rupture front propagated at subshear velocity. Indeed, fault-normal ground motion is consistent with near-field effects associated with S-wave arrivals ahead of a subshear rupture front (22, 23).

Based on GPS coordinates provided by the operating company, the camera was located approximately 124 km south of the mainshock hypocenter (Figure 1a). A key observation is the short time interval between the onset of ground motion (arrival 1) and the onset of slip (rupture arrival), measured as $\Delta t \approx 4.5$ s. Assuming an average rupture velocity of 3.6 km/s and a P-wave velocity of 6.2 km/s (Figure S2), one would expect a significantly longer delay, approximately $\Delta t \approx 14.4$ s. The unexpectedly short interval can be explained by two simplified scenarios.

First, the initial arrival may correspond to S waves. In this case, seismic radiation from the P-wave coda, whose onset likely occurred prior to the beginning of the recording, could have been minimal due to the recording site being located near the fault's nodal plane. This is theoretically expected and would explain the absence of clear P-wave signatures, implying that the rupture propagated at subshear speed for most of its extent (Figure S3). Second, it is possible that the rupture front initially propagated at supershear velocities, nearly reaching the local P-wave speed, before transitioning to subshear velocity near the observation site. In this case, the first arrival would be attributed to P waves and the second to S waves (Figure S3). More complex scenarios involving two-dimensional rupture front geometries along the fault may also explain the observed timing, but are beyond the scope of this discussion.

Estimate of the dynamic source parameters from the fault slip rate

Building on the pulse-like nature of the rupture, we apply the elastodynamic equilibrium condition to infer the evolution of shear stress from the slip rate measurements. Assume a 2D plane-strain shear (mode II) rupture propagating at a constant rupture velocity V_r along the fault, the shear stress $\tau(x)$ is related to the spatial distribution of slip rate $v(x)$ through the singular integral equation (24, 25):

$$\tau(x) = \tau_0 - \frac{\bar{\mu}}{2\pi V_r} \text{PV} \int_0^L \frac{v(\xi)}{x - \xi} d\xi \quad (1)$$

where τ_0 is the background stress, $\bar{\mu}$ is a scaled shear modulus, which depends on the rupture velocity V_r , and PV denotes the Cauchy principal value of the integral. To compute the shear stress evolution $\tau(x)$, we use a Chebyshev-based polynomial interpolation of the slip rate $v(x)$ (see Figure 4a), combined with Gauss-Chebyshev quadrature (26).

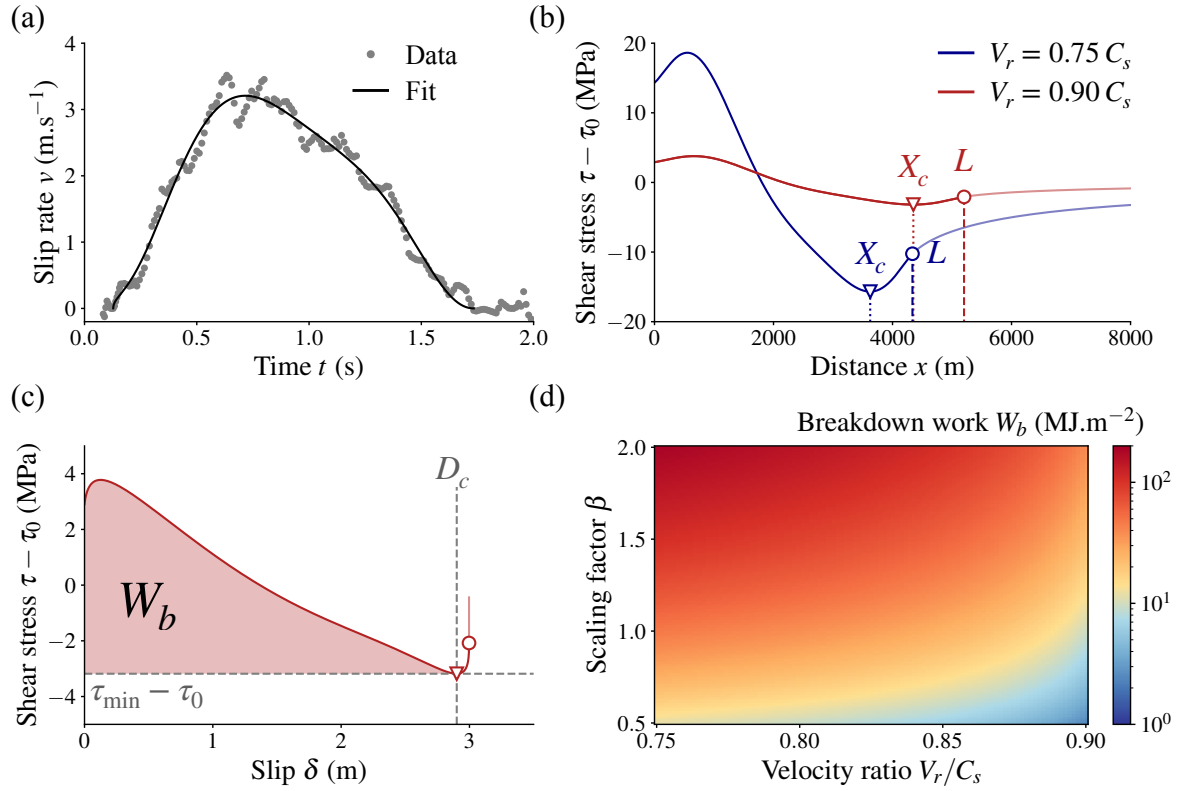


Figure 4: (a) Direct measurement of the fault slip rate (in grey circle markers) and Chebyshev-based fit (in black solid line). (b) Solution of the evolution of the shear stress change during the slip pulse propagation for both rupture scenario $V_r = 0.75 C_s$ (in solid blue line) and $V_r = 0.90 C_s$ (in solid red line). (c) Evolution of stress variation $\tau - \tau_0$ with slip, including the healing stage for $V_r = 0.90 C_s$. The breakdown work W_b (in shaded red area) is defined from an integral of the shear stress change $\tau - \tau_{\min}$ up to the critical slip distance $\delta = D_c$. (d) Impact of the uncertainty factor β defined as the ratio between the true slip rate on the fault and measured slip rate, and of the rupture velocity V_r on the values of W_b

Since the exact value of V_r is not known at this stage, we present results for two representative cases in Figure 4b: $V_r/C_s = 0.75$ and $V_r/C_s = 0.90$, corresponding to two rupture histories discussed in the supplementary material (Figure S4). As anticipated for pulse-like ruptures, we observe that the stress drop is followed by a restrengthening phase, which spans approximately 20 % of the pulse length. The dependence of the shear stress evolution on the rupture velocity V_r is also expected: since the slip rate profile is fitted directly from measurements, a lower rupture velocity V_r requires a larger stress drop $\Delta\tau$ to match the observed slip rates. In addition, in this framework, the size of the cohesive zone scales linearly with V_r . Because of that, the dynamic stress drop $\Delta\tau$ decreases and the cohesive zone X_c broadens as V_r increases. Specifically, we find $\Delta\tau = 7.0$ MPa and $X_c = 4350$ m for $V_r = 0.90 C_s$, compared to $\Delta\tau = 34.3$ MPa and $X_c = 3625$ m for $V_r = 0.75 C_s$. Examining the apparent stress-slip relationship in Figure 4c, we observe a linear decay of shear stress τ with slip δ , up to a critical slip value $D_c = 2.90$ m, which is consistent for both rupture velocities.

We then calculate the breakdown work $W_b = \int_0^{D_c} (\tau(\delta) - \tau_{\min}) d\delta$ associated with the slip pulse, integrating

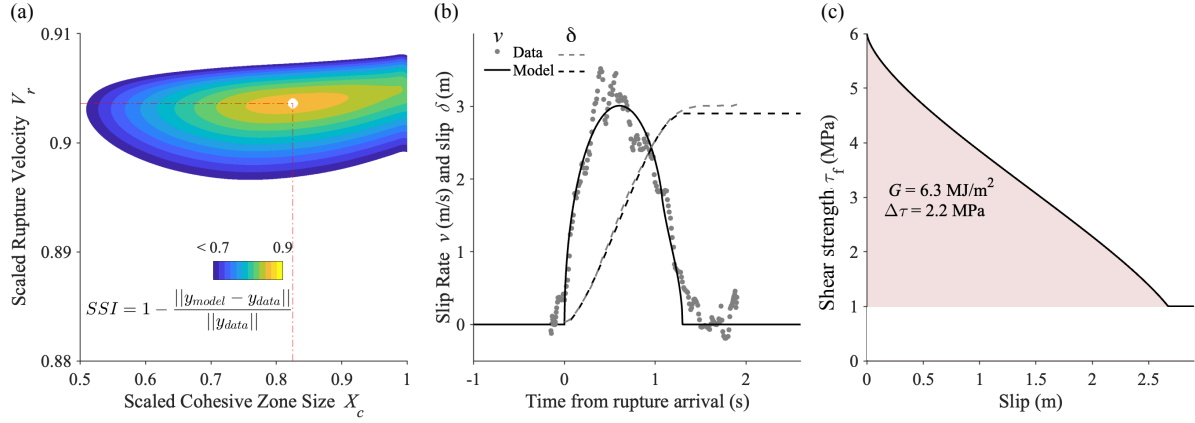


Figure 5: (a) Grid search for the best fitting scaled cohesive zone size, X_c/L , and scaled rupture velocity, V_r/c_s . The fit is measured using the Scaled Similarity Index defined above (b) Comparison, of slip and slip rate, between the best fitting model slip pulse and the observed one (c) Evolution of friction strength, τ_f , with slip, δ .

up to the point of minimum stress τ_{\min} , defined spatially at X_c and in cumulative slip at D_c (Figures 4b–c). The resulting values of W_b range from 9.5 MJ/m² for $V_r = 0.90, C_s$ to 46.9 MJ/m² for $V_r = 0.75, C_s$. These results suggest that the values of breakdown work are highly variable depending on the rupture velocity.

Because of that, we assess how uncertainties in the measurement of slip rate and rupture velocity affect the estimation of W_b . We explore a range of rupture speeds from $V_r = 0.75 C_s$ to $V_r = 0.90 C_s$, and vary the slip rate by a scaling factor β from 0.5 to 2 to account for possible errors in the estimated spatial scales. This parametric analysis quantifies how the retrieved breakdown work is sensitive to our measurement uncertainties and assumptions on rupture velocity.

To further constrain the rupture properties associated to our direct measurement of the fault slip rate, we propose to use a two-dimensional steady-state rupture pulse model (24). The model assumes a steady-state sub-Rayleigh rupture velocity V_r , and a constant-width breakdown zone in which the friction linearly decreases from the peak to the residual frictional strength ($f_p = 0.6$ and $f_r = 0.2$, respectively) behind the rupture front (Figure S5). We assume a nominal normal traction of 10 MPa by taking into account the shallow nature of the rupture. The slip pulse duration is fixed at $\delta t = 1.3$ s, (as estimated using pillar R_0 ; see Figure 3a, black solid line). We thus define the pulse length as $L = \delta t V_r$. Since the largest uncertainties are in the size of the scaled cohesive zone, X_c/L , and scaled rupture velocities, V_r/C_s we do a grid search for those parameters. We look for these parameters that produce the largest Signal Similarity Index, SSI, which is an Euclidean norm measure of how well the model slip pulse solution matches the measured one. As seen in Figure 5a, the largest SSI corresponds to $X_c/L = 0.83$ and $V_r/C_s = 0.903$, which provides the best fit (Figure 5b).

We now can obtain the full mechanical information of the slip-pulse measured from the CCTV camera.

The slip pulse had a cohesive zone size of about 3500 m and a rupture velocity of about 3250 m/s further constraining, and validating, the estimates from the traction changes calculated earlier. Based on the model we can also now infer the frictional strength evolution with slip and infer a strength drop, $\tau_p - \tau_r$, of 5 MPa, a stress drop, $\sigma_{xy}^0 - \tau_r$, of 2.2 MPa and an equivalent D_c estimate of about 2.67 m. We can now compute the energy release rate, G , associated with this slip pulse as $\int_0^{D_c} [\tau_f(\delta) - \tau_r] d\delta = 6.3 \text{ MJ/m}^2$, where $\tau_f(\delta)$ is the strength evolution with slip δ (Figure 5c). The energy release rate is also consistent with the measured breakdown work and is consistent with expectations for an earthquake of the size and geometry of the Mandalay event (27, 28, 29, 30).

Conclusions

We used the first known footage of surface rupture slip to provide the first direct measurement of the fault slip rate function during a natural earthquake. We show that the peak slip rate during the Mandalay rupture reached at least 3 m/s at the camera location, and lasted for approximately 1.3 seconds, with a slightly asymmetric slip-rate function. Despite some uncertainty on the slip and slip-rate measurements, our conclusion regarding the pulse-like nature of the rupture, and the shape of the slip-rate function remain robust. Using fundamental elastodynamic theory of propagating shear rupture, we provide a rapid, inversion-free estimate of the stress drop, strength drop, rupture velocity, cohesive zone size, breakdown work and the energy release rate of the short-duration, high-velocity slip pulse that swept past the camera.

Acknowledgments

The authors thank the anonymous individual who first shared the footage. F.P. thanks Barnaby Fryer and Federica Paglialunga for discussions and for proofreading the manuscript. S.L. and F.P. thanks Jean-Paul Ampuero and Françoise Courboux for valuable discussions.

Funding: F.P. acknowledge support from the European Union (ERC Starting Grant HOPE num. 101041966). H.S.B. acknowledge support from the ERC Consolidator Grant (865411), PERSISMO, for partial support of this work.

Author contributions: S.L. and F.P. conceived the study., S.L. and K.W.H. conducted the frame analysis based on satellite imaging, F.P., H.S.B. and M.L. estimated the rupture properties, C.T. and Q.B. analyzed the kinematic inversion from USGS and provided estimates of the wave speeds, S.L. and F.P. wrote the first draft of the manuscript, K.W.H. provided critical data for spatial scaling and validation. All authors contributed to discussions, interpretation of results, and reviewed the manuscript.

Competing interests: The authors declare no competing interests

Data and materials availability: All data and code necessary to directly reproduce our results will be made available upon acceptance of the manuscript.

References and Notes

1. J.-P. Avouac, From geodetic imaging of seismic and aseismic fault slip to dynamic modeling of the seismic cycle. *Annual Review of Earth and Planetary Sciences* **43** (1), 233–271 (2015).
2. A. Tarantola, B. Valette, Generalized nonlinear inverse problems solved using the least squares criterion. *Reviews of Geophysics* **20** (2), 219–232 (1982).
3. A. Saraò, S. Das, P. Suhadolc, Effect of non-uniform station coverage on the inversion for earthquake rupture history for a Haskell-type source model. *Journal of Seismology* **2**, 1–25 (1998).
4. I. A. Beresnev, Uncertainties in finite-fault slip inversions: to what extent to believe?(a critical review). *Bulletin of the Seismological Society of America* **93** (6), 2445–2458 (2003).
5. S. Hartzell, P. Liu, C. Mendoza, C. Ji, K. M. Larson, Stability and uncertainty of finite-fault slip inversions: Application to the 2004 Parkfield, California, earthquake. *Bulletin of the Seismological Society of America* **97** (6), 1911–1934 (2007).
6. P. M. Mai, *et al.*, The earthquake-source inversion validation (SIV) project. *Seismological Research Letters* **87** (3), 690–708 (2016).
7. N. G. Reitman, *et al.*, ArcGIS Experience Builder – Web App (2025), <https://experience.arcgis.com/experience/e40a6967c3ea42dd85bf44037e05482b>, consulted on May 15, 2025.
8. U.S. Geological Survey, Finite Fault – M 7.7 - 2025 Mandalay, Burma (Myanmar) Earthquake (2025), <https://earthquake.usgs.gov/earthquakes/eventpage/us7000pn9s/finite-fault>, consulted on May 16, 2025.
9. M. Vallée, J. Charléty, A. M. Ferreira, B. Delouis, J. Vergoz, SCARDEC: a new technique for the rapid determination of seismic moment magnitude, focal mechanism and source time functions for large earthquakes using body-wave deconvolution. *Geophysical Journal International* **184** (1), 338–358 (2011).
10. G. Bertrand, C. Rangin, Tectonics of the western margin of the Shan plateau (central Myanmar): implication for the India–Indochina oblique convergence since the Oligocene. *Journal of Asian Earth Sciences* **21** (10), 1139–1157 (2003).
11. N. Inoue, *et al.*, A multiple asymmetric bilateral rupture sequence derived from the peculiar tele-seismic P-waves of the 2025 Myanmar earthquake (2025).
12. T. H. Heaton, Evidence for and implications of self-healing pulses of slip in earthquake rupture. *Physics of the Earth and Planetary Interiors* **64**, 1–20 (1990).

13. D. Melgar, G. P. Hayes, Systematic Observations of the Slip Pulse Properties of Large Earthquake Ruptures. *Geophysical Research Letters* **44** (19), 9691–9698 (2017), doi:10.1002/2017GL074916.
14. H. Weng, J.-P. Ampuero, The dynamics of elongated earthquake ruptures. *Journal of Geophysical Research: Solid Earth* **124** (8), 8584–8610 (2019).
15. H. Weng, J.-P. Ampuero, Integrated rupture mechanics for slow slip events and earthquakes. *Nature Communications* **13** (1), 7327 (2022).
16. S. Minson, M. Simons, J. Beck, Bayesian inversion for finite fault earthquake source models I—Theory and algorithm. *Geophysical Journal International* **194** (3), 1701–1726 (2013).
17. H. N. Razafindrakoto, P. M. Mai, Uncertainty in earthquake source imaging due to variations in source time function and earth structure. *Bulletin of the Seismological Society of America* **104** (2), 855–874 (2014).
18. I. A. Beresnev, Choices of slip function and simulated ground motions. *Pure and Applied Geophysics* **181** (6), 1859–1869 (2024).
19. G. Lykotrafitis, A. J. Rosakis, G. Ravichandran, Self-healing pulse-like shear ruptures in the laboratory. *Science* **313** (5794), 1765–1768 (2006).
20. S. Nielsen, R. Madariaga, On the Self-Healing Fracture Mode. *Bulletin of the Seismological Society of America* **93** (6), 2375–2388 (2003).
21. E. Tinti, E. Fukuyama, A. Piatanesi, M. Cocco, A Kinematic Source-Time Function Compatible with Earthquake Dynamics. *Bulletin of the Seismological Society of America* **95** (4), 1211–1223 (2005).
22. E. M. Dunham, R. J. Archuleta, Near-source ground motion from steady state dynamic rupture pulses. *Geophysical Research Letters* **32** (3) (2005).
23. T. Gabrieli, Y. Tal, Lab earthquakes reveal a wide range of rupture behaviors controlled by fault bends. *Proceedings of the National Academy of Sciences* **122** (17), e2425471122 (2025).
24. J. R. Rice, C. G. Sammis, R. Parsons, Off-Fault Secondary Failure Induced by a Dynamic Slip Pulse. *Bulletin of the Seismological Society of America* **95** (1), 109–134 (2005), doi:10.1785/0120030166, <https://pubs.geoscienceworld.org/ssa/bssa/article/95/1/109/146908/off-fault-secondary-failure-induced-by-a-dynamic>.
25. N. Brantut, Analysis of Stress in the Cohesive Zone, Dissipation and Fracture Energy During Shear Rupture Experiments. *Geophysical Research Letters* **52** (9), e2024GL113972 (2025), doi:10.1029/2024GL113972, <https://onlinelibrary.wiley.com/doi/abs/10.1029/2024GL113972>.

26. R. C. Viesca, D. I. Garagash, Numerical methods for coupled fracture problems. *Journal of the Mechanics and Physics of Solids* **113**, 13–34 (2018).
27. R. E. Abercrombie, J. R. Rice, Can observations of earthquake scaling constrain slip weakening? *Geophysical Journal International* **162** (2), 406–424 (2005).
28. E. Tinti, P. Spudich, M. Cocco, Earthquake fracture energy inferred from kinematic rupture models on extended faults. *Journal of Geophysical Research: Solid Earth* **110** (B12) (2005).
29. S. Nielsen, *et al.*, G: Fracture energy, friction and dissipation in earthquakes. *J. Seismol.* **20**, 1187–1205 (2016), doi:10.1007/s10950-016-9560-1.
30. M. Cocco, *et al.*, Fracture energy and breakdown work during earthquakes. *Annual Review of Earth and Planetary Sciences* **51** (1), 217–252 (2023).